



Scalable Synthesis of Li₂S Nanocrystals for Solid-State Electrolyte Applications

Yangzhi Zhao, William Smith, and Colin A. Wolden 1,2,*,z

¹Materials Science Program, Colorado School of Mines, Golden, Colorado 80401, United States of America
²Department of Chemical and Biological Engineering, Colorado School of Mines, Golden, Colorado 80401, United States of America

Lithium sulfide (Li_2S) is a key component and major cost driver for sulfide-based solid-state electrolytes. However, this material is not commercially available in nanocrystal form. We previously demonstrated solution-based synthesis of Li_2S nanocrystals (NCs) with tunable size in a small Parr reactor and validated their potential as cathode active materials. Herein, we report on the scale-up of both the synthesis and purification steps, generating meaningful quantities for solid-state electrolyte formation. Use of a bubble column reactor significantly increased production capacity by two orders of magnitude, from~100 mg/batch to >10 g/batch. An evaporator/condenser and fluidized bed with corresponding capacity were introduced for solvent evaporation and annealing, respectively. Intrinsic purity, thermal stability, and morphology of those NCs are characterized by XRD, TGA, and SEM respectively. It is shown that the NC size and purity could be tuned by varying the annealing temperature. $\text{Li}_2\text{S-P}_2\text{S}_5$ based glassy electrolytes formed by a combination of ball milling and cold pressing were used to illustrate the benefits of these Li_2S NCs. It was shown that Li_2S NCs reduced the mechanical ball mixing time required to make $\text{Li}_2\text{S-P}_2\text{S}_5$ based glasses by at least 70% relative to commercial Li_2S micro-powders. $70\text{Li}_2\text{S-}30\text{P}_2\text{S}_5$ glassy electrolytes were fabricated by cold pressing at various pressures and characterized by impedance spectroscopy and chronoamperometry. SSEs formed at the optimum condition exhibited high ionic conductivity ($\sim 10^{-5}$ s cm⁻¹), low electronic conductivity ($\sim 10^{-10}$ s cm⁻¹), and reasonable activation barrier (~ 35 kJ mol⁻¹). These properties were comparable to leading reports in the literature, validating the use of our material for solid-state electrolyte fabrication.

© 2020 The Author(s). Published on behalf of The Electrochemical Society by IOP Publishing Limited. This is an open access article distributed under the terms of the Creative Commons Attribution Non-Commercial No Derivatives 4.0 License (CC BY-NC-ND, http://creativecommons.org/licenses/by-nc-nd/4.0/), which permits non-commercial reuse, distribution, and reproduction in any medium, provided the original work is not changed in any way and is properly cited. For permission for commercial reuse, please email: oa@electrochem.org. [DOI: 10.1149/1945-7111/ab6e3f]

Manuscript submitted December 4, 2019; revised manuscript received January 14, 2020. Published February 12, 2020. This paper is part of the JES Focus Issue on Challenges in Novel Electrolytes, Organic Materials, and Innovative Chemistries for Batteries in Honor of Michel Armand.

Supplementary material for this article is available online

The past decade has seen tremendous progress in the development of solid-state electrolytes (SSEs) and all-solid-state batteries (ASSBs) in attempts to expand deployment of vehicle electrification. 1,2 The capacity of current lithium ion batteries (LIBs) is constrained by its use of a flammable liquid electrolyte, which also introduces safety concerns. ASSBs can be manufactured in a more compact form such as bi-polar stacking system with notably improved specific power and capacity.3 Moreover, SSEs could potentially provide better compatibility with Li metal anode with appropriate interfacial engineering, further maximizing the full-battery energy density. Sulfide-based SSEs are very attractive due to their ease of processing, good electrochemical window, and high ionic conductivity with some materials surpassing the room temperature ionic conductivity of liquid electrolytes.4 Example SSEs and representative ionic conductivity values from within the Li₂S-P₂S₅ (LPS) system include glassy electrolytes ($\sim 10^{-5} \, \mathrm{s \ cm^{-1}}$), $^5 \, \mathrm{Li_3PS_4}$ ($\sim 10^{-4} \, \mathrm{s \ cm^{-1}}$), and the metastable Li₇P₃S₁₁ phase ($\sim 10^{-2} \, \mathrm{s \ cm^{-1}}$). $^6 \, \mathrm{Li_{10}GeP_2S_{12}}$ and argyrodite (Li₆PS₅X, X = Cl, Br, I) are related LPS-based superionic conductors with reported values on the order of $10^{-2} \, \mathrm{s \ cm^{-1}}$ and $10^{-3} \, \mathrm{s \ cm^{-1}}$, respectively.^{7,3}

 ${\rm Li_2S}$ is the key component and a major cost driver in sulfide-based SSE synthesis. At present the cost of research grade ${\rm Li_2S}$ is exorbitant (${\sim}$15,000~{\rm kg}^{-1}$). This reflects current production methods which rely on energy intensive carbothermal reduction techniques that create ${\rm Li_2S}$ as a bulk powder with significant impurities. While the costs are reduced an order of magnitude at bulk, they remain prohibitive and inhibit expansion of technologies based on this material. In the approach described here the dominant cost is that of the Li metal precursor, which has traded at ${\sim}$115~{\rm kg}^{-1}$ for the past year. A low energy process that efficiently converts

this into Li₂S would be expected to make this material at cost of \$50–100 kg⁻¹ Li₂S. Solid-state electrolytes are typically formed by mixing and annealing constituent powders, and smaller crystals have been correlated with reduced thermal budgets and improved interfacial resistance. ¹⁰ It is expected that such small-sized particles would also be beneficial for emerging liquid–phase approaches for synthesis of superionic conductors such as Li₇P₃S₁₁^{11–13} and argyrodites. ^{14–16}

Our group has developed a solution-based approach for the direct synthesis of Li₂S by contacting a lithium precursor solution with the industrial waste hydrogen sulfide (H₂S). First, lithium reacts with an alcohol to form metalorganic precursor solution, releasing pure H₂ as a byproduct.¹⁷ Next, purified H₂S (i.e. rotten eggs odor) is bubbled through the solution, forming Li₂S. Depending on choice of cosolvent Li₂S NCs either precipitate directly out of solution¹⁸ or are recovered in a subsequent evaporation step. ¹⁹ In either case the alcohol solution can be recovered and recycled. The net reaction of this green process, $2Li + H_2S \rightarrow Li_2S + H_2$, has numerous advantages. First, H₂S is a major liability for the oil and gas industry and this process results in its complete abatement (>99.99%). Second, the valuable hydrogen within H₂S is completely recovered and may be used to supply clean burning fuel cells. Third, the Li₂S is directly produced in the desired nanocrystalline morphology for battery applications. Finally, due to the favorable energetics this chemistry occurs instantaneously at room temperature with an atom economy approaching unity, meaning there are no deleterious side reactions and the energy requirements are minimal.

The process was first developed using reactive precipitation, which facilitates NC recovery. However, only $\sim 85\%$ of the lithium used is directly recovered, with losses due to handling and Li₂S remaining dissolved in solution. In addition, the resulting NCs were relatively large (>100 nm) with nonideal morphology. Although cathodes made from Li₂S NCs by reactive precipitation were superior to commercial Li₂S counterparts, they still fell short of

^zE-mail: cwolden@mines.edu

the theoretical capacity (1166 mAh g $^{-1}$ Li $_2$ S). 20 Recently we introduced a variation by changing the co-solvent so that Li $_2$ S remains fully dissolved, with NCs recovered in a subsequent evaporation step. Using this approach, it was shown that NC size could be tuned (5 – 25 nm) by appropriately controlling the solution chemistry and/or subsequent processing. Cathodes made from NCs <10 nm in size had capacity that approached the theoretical value and displayed good cyclability and rate capability. 19

The materials synthesis, solvent evaporation and materials annealing/purification from previously developed solvo-evaporation were conducted using a Parr reactor and tube furnace, with typical yields of $\sim\!100$ mg/batch. These quantities were sufficient for cathode fabrication but fall short of the material required for practical synthesis of SSEs. In this paper we describe the scale up of this process using scalable unit operations including bubble columns and fluidized beds. Using these approaches the synthetic capacity was increased by two orders of magnitude to quantities $>\!10$ g batch $^{-1}$. In addition, it was shown that the co-solvent DMF could be eliminated, decreasing both the temperature and time needed for solvent evaporation. The intrinsic material properties were evaluated by SEM, XRD, and TGA. Finally, the benefits of this material for SSE formation were demonstrated using $70 \text{Li}_2 \text{S} - 30 \text{P}_2 \text{S}_5$ glassy electrolytes as a model system.

Experimental

Reagents.—Ethanol (EtOH, CH_3CH_2OH , anhydrous, $\geqslant 99.5\%$), N,N-dimethylformamide (DMF, $HCON(CH_3)_2$, anhydrous, 99.8%), and phosphorus pentasulfide (P_2S_5 , 99%) were purchased from Sigma-Aldrich. Lithium foil (Li, 0.75 mm thick \times 19 mm wide, 99.9% trace metals basis) was purchased from Alfa Aesar. A specialty mixture of 10% of H_2S in Ar (Scott Specialty Gasses) and UHP argon (99.999% purity) were employed. All purchased chemicals were used as received without further purification.

Pellet formation.—Li $_2$ S and P $_2$ S $_5$ were measured based on molar ratio of 7:3 and mixed by mortar and pestle in a glovebox (LC-1, LC Technology Solutions Inc.) The resulting mixture was then transferred in ZrO $_2$ ball mill jar (40 ml) with three ZrO $_2$ balls (10 mm diameter), sealed, and mounted in a high energy ball mixer (SPEX, Mixer/Mill 8000 M). After sufficient ball mixing 150 mg of the amorphous mixture was loaded homogenously in a die with 1/2-inch diameter. Pellets were formed with the thickness of 0.7–0.8 mm by

cold-pressing using a hydraulic press (YLJ-15L, MTI Corp.). Pellets were pressed by increasing pressure in 100 MPa increments to the target pressure, stabilizing at each increment for 1 min before moving to the next. Samples were held for 2 min at the final target pressure. Relative density is calculated by measuring the mass and volume of the pellet, normalized to the literature value of 1.95 g cm⁻³. Each sample has been reproduced at least 10 times by following the same procedure. The same sample was always used to test EIS and chronoamperometry.

Materials characterization.—X-ray diffraction (XRD) was measured on a Philips X'Pert X-ray diffractometer with Cu K α radiation $(\lambda = 0.15405 \text{ nm})$. Samples were prepared on a quartz slide with a drop of mineral oil covering the material to prevent undesired reaction with ambient moisture. Thermal gravimetric analysis (TGA) was performed with a TGA Q50 from TA Instruments. Approximately 5 mg sample was inserted into an alumina pan then loaded into the furnace under Ar flow. Isothermal tests were performed by ramping to 200 °C in 1 min, then holding for 2 h. Field emission scanning electron microscopy (FESEM) images of synthesized Li₂S powder and solid-electrolyte pellets were taken on a JEOL JSM-7000F FESEM instrument. An accelerating voltage of 5 kV was used for image capturing. The cross-section morphology was obtained from fractured pellets without further surface polishing in order to preserve the true morphology. Finally, particle-size distribution of the purified Li₂S was conducted by small-angle X-ray scattering (SAXS). The measurement was performed under vacuum with a line collimation instrument from Anton Paar equipped with PW3830 stand-alone laboratory X-ray source from PANalytical (Cu K α radiation, $\lambda = 0.15405$ nm, operated at 40 kV & 50 mA) and Mythen2 R microstrip detector from Dectris. SAXS samples were prepared by placing approximately 20 mg of powder in a 1 cm² sample holder, which was then sealed between two pieces of Scotch Magic[™] Tape. The sample was kept in an argon environment right before conducting SAXS measurements. SAXS data was background subtracted and desmeared using SAXSQuant (Anton Paar) and fit to a particle-size distribution in the range of 2.5 to 100 nm using the Irena toolbox (developed by Argonne National Lab) in Igor Pro from Wavemetrics, Inc.

Electrochemical testing.—Blocking electrodes for electrochemical characterization were formed by magnetron sputtering (AJA

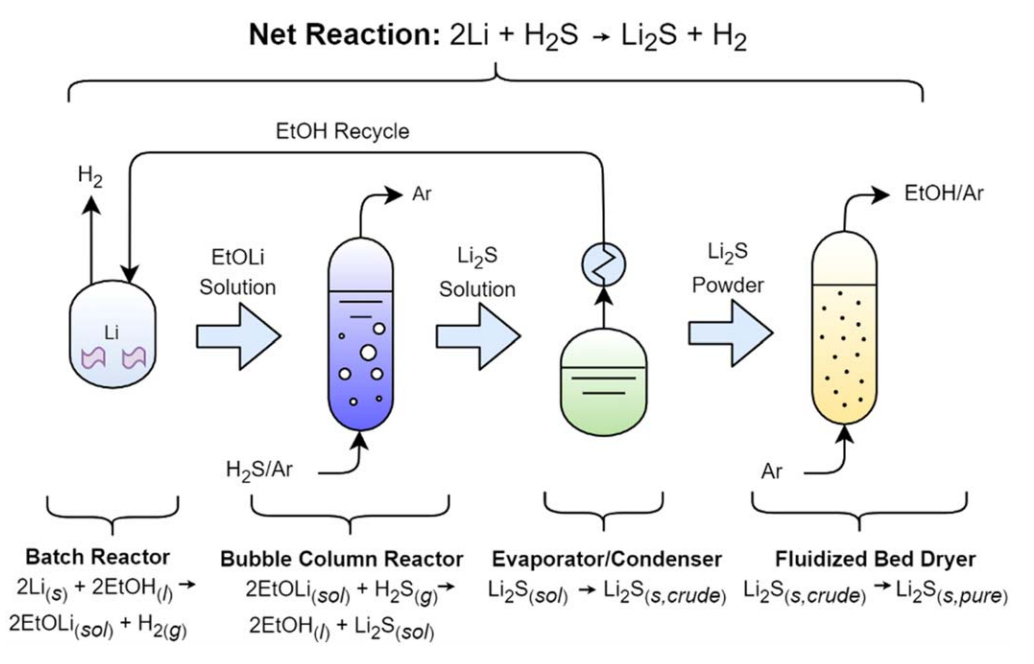


Figure 1. Process flow diagram of Li₂S NC synthesis and purification.

International Inc.) of $\sim\!100\,\mathrm{nm}$ of aluminum to each side using $72.5\,\mathrm{mW\,cm^{-2}}$ at 5.98 mtorr in an Ar ambient. Connections to analytical instrumentation were made using silver wires (0.02 in diameter, $4\,\mathrm{N}$ purity, ESPI) attached using conductive adhesive electro-bond 07 (ConductiveX) cured at room temperature. A Gamry Interface 1000E potentiostat was interfaced through the glovebox and used for electrochemical impedance spectroscopy (EIS) and chronoamperometry measurements. EIS measurement was conducted in the frequency range of $1\,\mathrm{Hz}$ to $1\,\mathrm{MHz}$. Chronoamperometry was performed by applying a step voltage of $500\,\mathrm{mV}$ DC and running for more than 20 min to obtain a steady state current measurement. Results reflect the average and standard deviation of at least 10 pellets at ech condition. Temperature was controlled by immersing the pellet in a heated sand bath for T-dependent EIS measurements.

Results and Discussion

Li₂S synthesis.—In our previous work precursor solutions were prepared by reacting lithium with ethanol in a 1:8 molar ratio to obtain lithium ethoxide, and then adding appropriate amounts of DMF to create clear solutions varying from 0.4 –1.6 M. ¹⁹ Li₂S was produced by bubbling a stoichiometric quantity of H₂S through the solution in a small Parr reactor. Li₂S NC were recovered by transferring aliquots of the resulting solution to a tube furnace and first evaporating the solvent and then annealing under flowing Ar. Figure 1 displays the scaled up process flow and identifies the key unit operations involved. The synthesis step is now conducted in a bubble column reactor, which are widely used in the chemical process industry as gas-liquid-solid contactors because of their simple construction and operation. 22 Instead of a tube furnace, NCs are recovered in an evaporator/condenser, which enables recovery and recycling of the solvents. Finally, the annealing step, which is critical to fully removing solvents and creating the purity required for electrochemical applications, is conducted in a fluidized bed dryer. Details on the construction and operation of the individual unit operations follow.

To prepare the precursor solution for large-scale synthesis, two 550 ml aluminum containers were first charged with lithium metal and ethanol, respectively, in an Ar-filled glovebox. Then, pressurized Ar was used to transfer ethanol to the lithium container to initiate the reaction. H2 gas was evacuated from the reactor headspace for analysis with residual gas analyzer. (Fig. S1 is available online at stacks.iop.org/JES/167/070520/mmedia) Due to the reaction exothermicity ($\Delta H_{rxn} = -175 \text{ kJ mol}^{-1}$), the reactor was immersed in an ice bath and solvent temperature remained at 40 °C or lower throughout reaction. At large-scale production, it is possible that this waste heat could be recycled for use elsewhere in the process-such as in the solvent evaporation step-further reducing the energy requirements. Pressurized Ar was again used to transfer precursor solution into the bubble column, and then to transfer Li₂S solution out of the column into the solvent evaporator. All synthetic steps except the initial charging of the precursor solution containers with lithium metal and ethanol were carried out in sealed containers with Ar blanket outside of a glovebox.

Our initial approach was to directly transfer this process from the Parr reactor to a bubble column which was previously employed for Li₂S NC synthesis by reactive precipitation. ¹⁸ In the case of reactive precipitation it was necessary to introduce fluorinated pump oil (Fomblin) at the base of the column to prevent NCs from clogging the sparger. In the current approach Li₂S remains dissolved in solution so the use of Fomblin is not required. However, without Fomblin the column experienced serious problems with foaming once the flowrate was increased beyond 60 sccm (superficial velocity $u_0 = 0.3 \text{ cm s}^{-1}$). At 100 sccm the entire column is occupied by foam as shown in Fig. 2. This issue was attributed to the fine pore sizes (2–40 µm) of the sintered stainless-steel discs used as the sparger. Replacing the sintered disk sparger with a mesh filter gasket with a pore size of 105 µm enabled flowrates up to 500 sccm ($u_0 =$

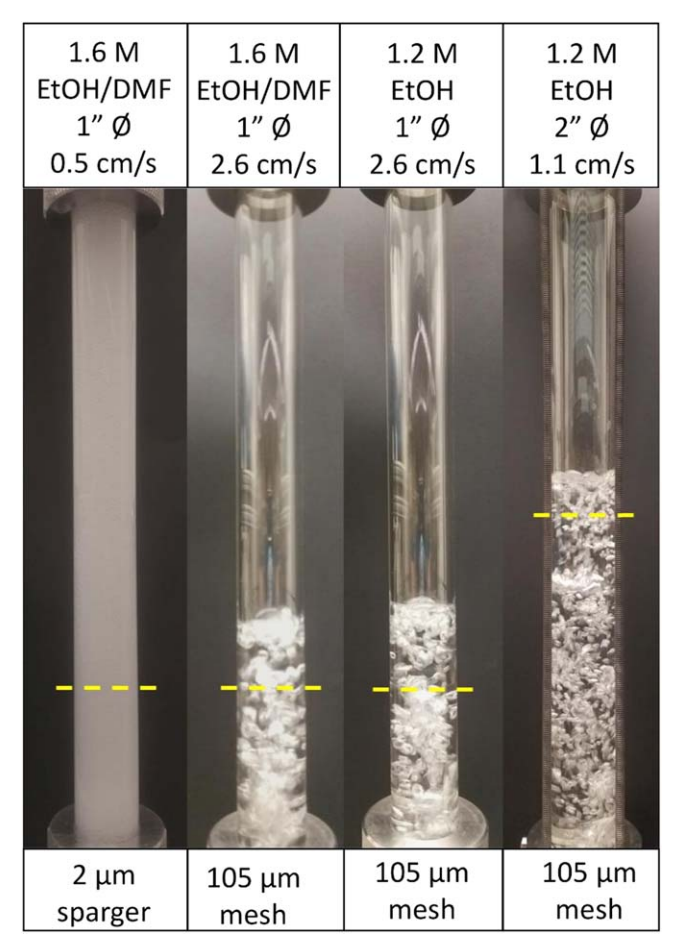


Figure 2. Photographs of the bubble column reactor (1" columns left three images, 2" column right image) under different operating conditions. The dashed lines indicate the approximate liquid level prior to gas introduction.

2.6 cm s⁻¹). The use of DMF as a co-solvent has the advantage in that it enabled greater solubility for lithium ethoxide, but it also increases temperature and energy requirements in the NC recovery step due to its higher boiling point. Elimination of DMF reduced the maximum concentration of the lithium ethoxide from 1.6 M to 1.2 M to remain completely dissolved. It has little effect on operation of the bubble column reactor as good bubble dispersion with minimal holdup was observed.

The scalability of the bubble column approach was then demonstrated by fabricating a 2" OD (1.75" ID) column which enabled the flowrate to be increased to 1000 sccm ($u_0 = 1.1 \text{ cm s}^{-1}$). The bubble dynamics and size in the 1" and 2" columns are similar. (Fig. 2) Gas holdup (defined as $\varepsilon = \frac{V_{Liquid+Gas} - V_{Liquid}}{V_{total}}$) decreased by 9% from the 1" to 2" column. This difference is attributed to a difference in bubbling flow regimes. Small diameter bubble columns with high gas velocities occupy the plug-flow regime while larger diameter columns with more moderate gas velocities occupy the homogeneous regime.²³ With the introduction of the 2" column, the solution volume was increased from 40 ml to 400 ml, and the rate of Li₂S synthesis was doubled from 6 to 12 g h⁻¹. Based on superficial velocity it is expected that the rate could be at least doubled, but experimentally we were limited by the capacity of the mass flow controllers available on hand (1000 sccm). The use of the 2" column allowed for the synthesis of large batches of Li₂S on the order of 10 g each.

NC recovery and purification.—Li₂S NCs were recovered by solvent evaporation followed by a mild annealing step that was found important to ensure complete solvent/impurity removal and achieve optimal electrochemical performance. Previously these steps

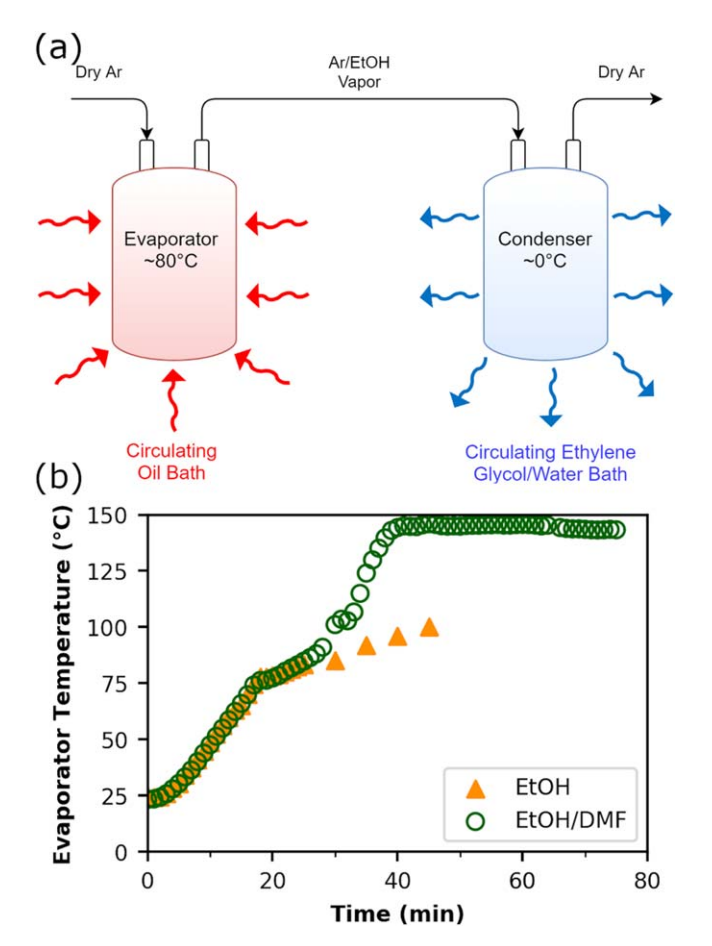


Figure 3. (a) Schematic of evaporation-condensation process for EtOH system. (b) Evaporator liquid-vapor temperature during the evaporation step for both EtOH/DMF and EtOH solvent systems.

were conducted in a tube furnace under Ar flow after transferring small aliquots of solution to a ceramic dish. To handle the increased volume of materials, an evaporator-condenser and a fluidized bed were designed and constructed to conduct drying and annealing, respectively.

To evaporate solvent, the full 400 ml Li₂S solution was transferred to an aluminum container, which was then heated in a circulating oil bath at a rate of ~4 °C min⁻¹ under 100 sccm Ar flow. Exiting vapor was sent through a condenser operating at around 0 °C in a circulating ethylene glycol/water bath. (Fig. 3a) Solvent recovery from the evaporation process was about 92%, and it is expected a recycling scheme could be developed for large-scale production, therefore improving the sustainability and material economy of the overall process. Liquid-vapor temperature within the evaporator was monitored throughout and the endpoint for evaporation was determined by observing the temperature exceed the boiling point of the solvent. A graphical representation of this process for both the ethanol and ethanol/DMF systems is shown in Fig. 3b. The elimination of DMF decreased both the temperature and time needed for solvent evaporation. Following evaporation, the evaporator was allowed to cool to room temperature then transferred into a glovebox to recover Li₂S powder.

Further drying/annealing of the recovered powder was necessary to remove all solvent and any volatile impurities, as well as to improve the crystallinity of the material. As shown by ourselves and others, and an analysis of the material. It is speculated that this temperature is required for the decomposition and removal of the solvated adduct Li₂S•CH₃CH₂OH. The Li₂S powder recovered from the evaporator was transferred to a 300 ml

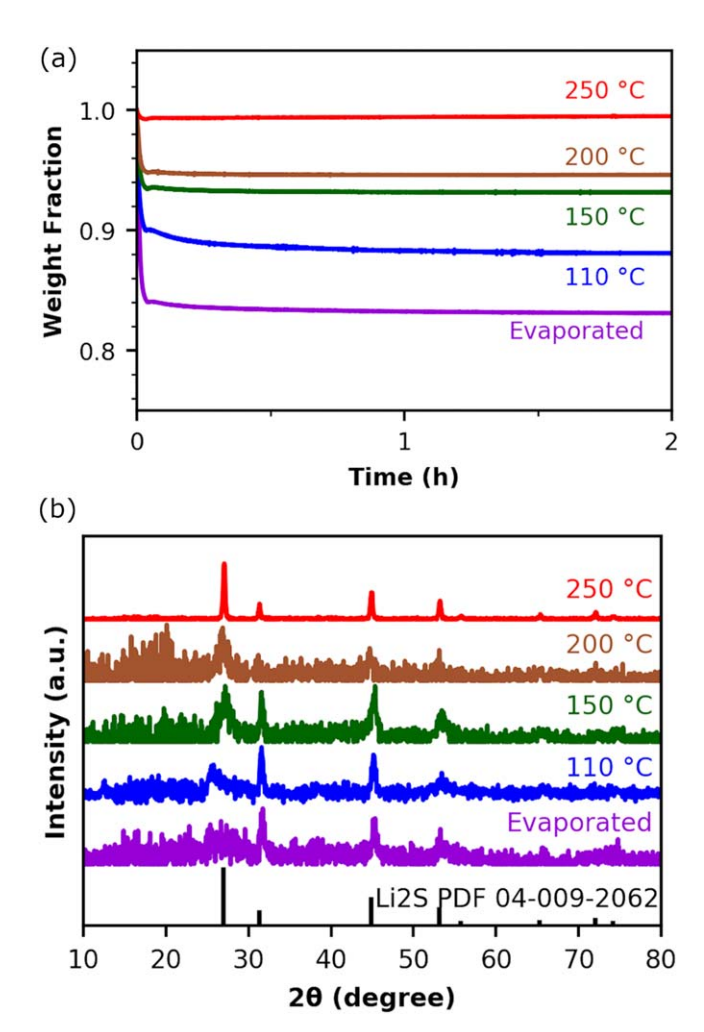


Figure 4. (a) Isothermal TGA scans at 200 °C on material annealed in the fluidized bed at selected temperatures. (b) XRD of material after evaporation and fluidized bed annealing at different temperatures.

steel cylinder fluidized bed, sealed by 2 μm sintered steel filter gaskets to prevent material loss. The supplemental information includes a video of the fluidized bed operated in a 1" glass column for visualization purposes. The critical gas velocity for achieving fluidization was measured to be \sim 2.5 cm s⁻¹ by observation of operation in the 1" glass column, and the Ar flowrate was adjusted accordingly to use this superficial velocity in the stainless steel chambers. The steel cylinder was oriented vertically in a cylindrical furnace set to the desired temperature for 2 h. Following the annealing step, the overall yield of the synthesis and processing was 93% with losses mainly attributed to transfers between steps and handling of the powder.

NC characterization.—Li₂S NCs recovered from solvent evaporation at $\sim\!80\,^{\circ}\text{C}$ then purified in the fluidized bed were characterized by TGA, XRD, and SEM. To determine the annealing temperature required to achieve high purity NCs annealing experiments were conducted in the fluidized bed at several different temperatures and the resulting powders were characterized by XRD and isothermal TGA experiments at 200 °C. (Fig. 4) The material directly from the evaporator experienced a $\sim\!17$ wt. % loss in the TGA experiments (Fig. 4a). This is not unexpected because while the material appeared nominally dry upon removal there was certainly additional solvent present in pores or adsorbed on the surface of the nanostructured material. The amount of weight loss after annealing decreases with the temperature of the fluidized bed as expected. It appears that a set point of 250 °C is required to achieve

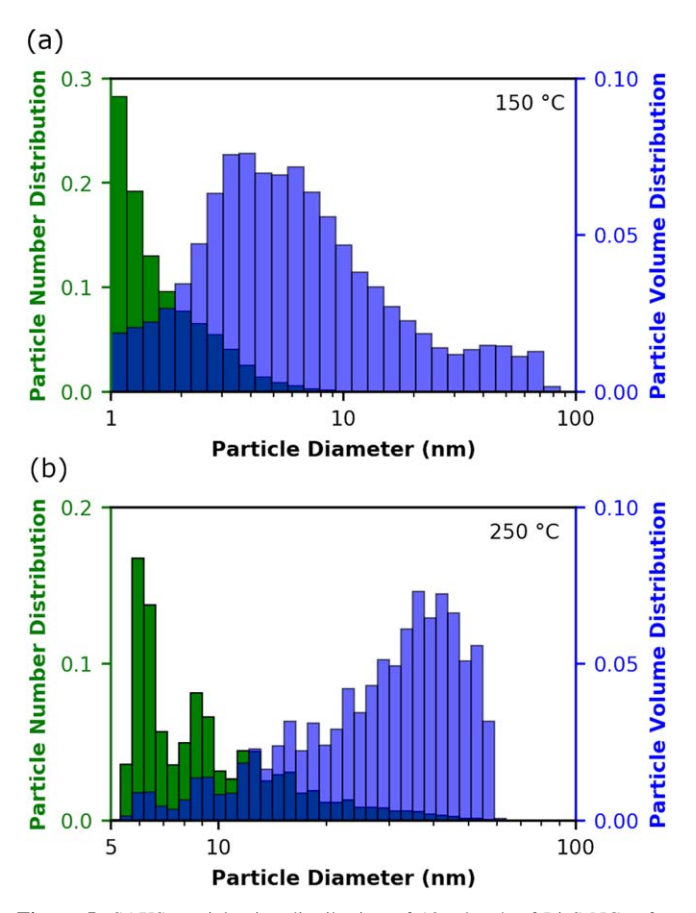
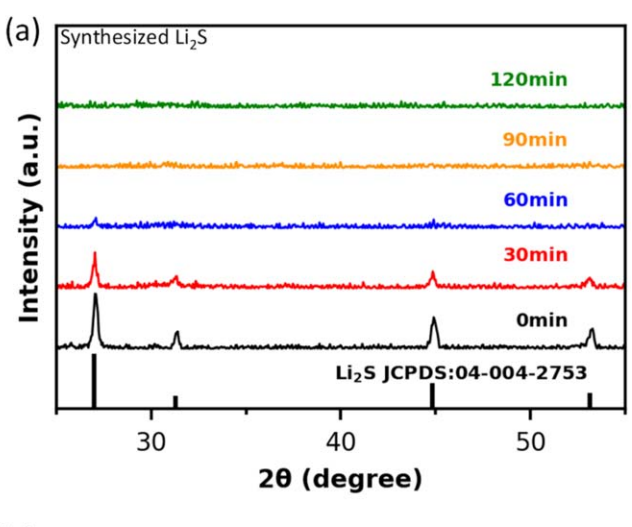


Figure 5. SAXS particle size distribution of 10 g batch of Li $_2$ S NCs after annealing at (a) 150 °C and (b) 250 °C for 2 h each.

phase-pure Li $_2$ S without additional weight loss which the growth of size might help. Note that this temperature is the setpoint of the furnace. Due to losses and the endothermic nature of evaporation the temperature experienced by the NCs within the bed is somewhat lower but that could not be directly measured. Figure 4b shows XRD of the material obtained after each annealing step. The material from the evaporator shows some degree of crystallinity, with preferential orientation in the (200) direction as evidenced by the unusually large peak at $2\theta = 31.3^{\circ}$. Annealing up to T = 200 °C does little to change the patterns, characterized by broad peaks characteristic of sub-10 nm crystallites as estimated by the Scherrer equation. Annealing at 250 °C results in an abrupt improvement in crystallinity, a loss of preferential orientation, and ~ 30 nm crystallites as estimated by the Scherrer equation.

To more accurately assess the particle size distribution of the Li₂S NCs at 10 g scale, SAXS was performed after annealing at 150 $^{\circ}\text{C}$ and 250 $^{\circ}\text{C}$ and the scattering data was fit to a particle size



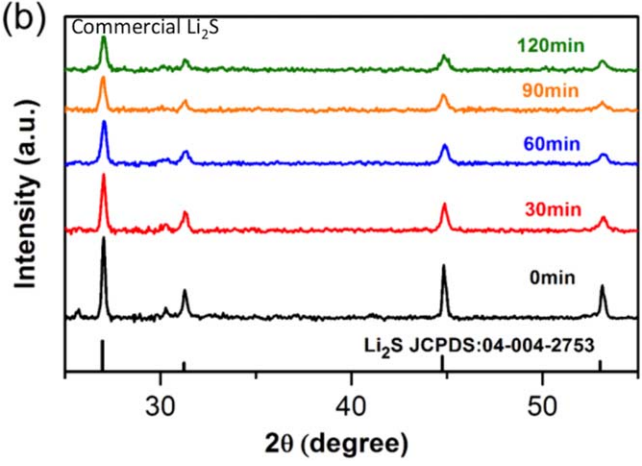


Figure 7. XRD of $70\text{Li}_2\text{S}$ - $30\text{P}_2\text{S}_5$ as a function of ball-milling time for (a) as-synthesized Li₂S NCs and (b) commercial Li₂S.

distribution. (Fig. 5) While the particle volume distribution is broader for both cases than that exhibited in previous work conducted with small quantities, ¹⁹ the scattering for material annealed at 150 °C still shows clear evidence of sub 10 nm particles with an average size around 9 nm with the vast majority of number of particles having a diameter less than 10 nm. After annealing at 250 °C, the particle size distribution shifts to larger values, with a volume-weighted average around 44 nm, which is in acceptable agreement with the Scherrer estimate. The uniformity of particles is indicated by polydispersity index (PDI), which is simply the mean size based on volume divided by the mean size based on number. The number-weighted average diameter is 31 nm resulting in a low PDI of 1.4.

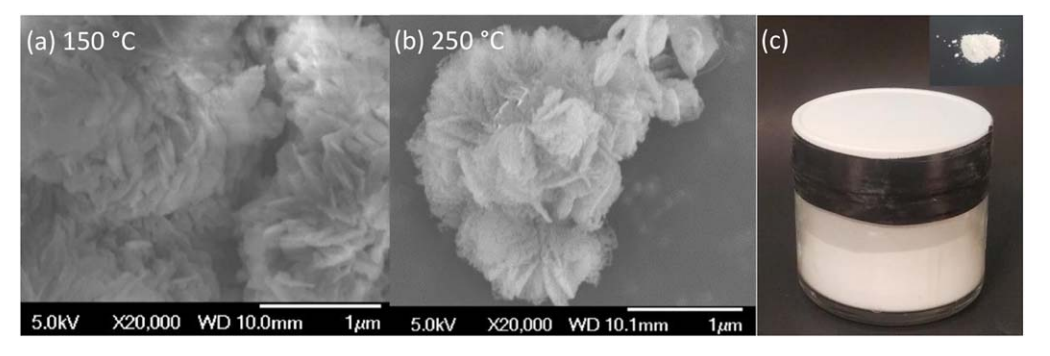


Figure 6. SEM image of the Li₂S NCs annealed at (a) 150 °C and (b) 250 °C showing unique nanoflower morphology. (c) Image of a 10 g batch of Li₂S NCs with additional image (inset) to show details.

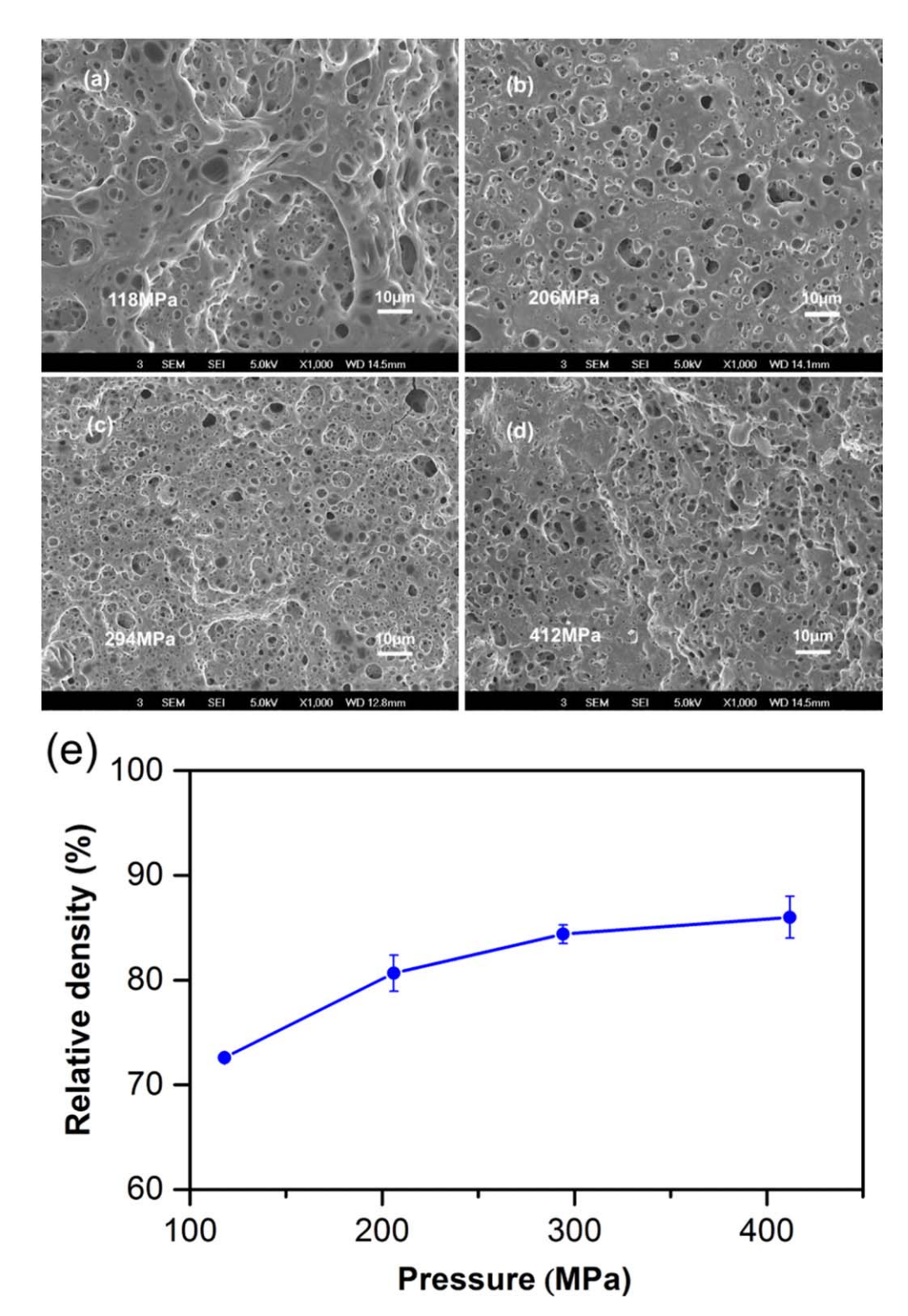


Figure 8. (a)—(d) Cross-section SEM images (×1000 magnification) of pellets cold-pressed at different pressures, and (e) densification demonstrated by relative density of cold pressed samples as a function of pressing pressure.

Finally, the morphology of the Li₂S NCs was investigated via SEM. Previous work revealed that a nanoflake morphology resembling flower petals was crucial to achieve maximum electrochemical activity. ¹⁹ Figure 6 shows an SEM image of the Li₂S powder after annealing at 150 °C and 250 °C confirming the presence of this nanoflower morphology at scale along with an image of the bulk powder for reference.

Glassy electrolyte fabrication.—The quality of the materials produced in the foregoing bubble column/fluidized bed was validated by the fabrication and characterization of $70\text{Li}_2\text{S}-30\text{P}_2\text{S}_5$ glassy electrolytes. First, P_2S_5 was mixed with either commercial ($\text{Li}_2\text{S}(c)$) or synthesized $\text{Li}_2\text{S}(c)$) using a mortar and pestle and then subjected to ball milling. Figure 7 displays XRD patterns of both mixtures as a function of time. The presence of crystalline

phases are clearly observed in the initial mixtures, and the peak of the sample using Li₂S(s) is slightly broader than that of Li₂S(c) equivalent, confirming the initial crystal size difference from two samples. The crystalline phase of Li₂S(s)-P₂S₅ mixture is rapidly attenuated and the mixture becomes completely amorphous after only 90 min. However, with commercial Li₂S, the process is much slower, and the mixture remains predominantly crystalline after 120 min ball mixing. To achieve the completely amorphous phase, 300 min ball mixing in total has been used on Li₂S(c)-P₂S₅ mixture as it is shown in Figs. S2, S3. It is noticed that ZrO2 impurities appear in the mixture due to direct collision of ZrO₂ balls and jar. Therefore, because of small crystal size of synthesized Li₂S nanopowders, the ball mixing time has been reduced by >70%, which significantly facilitates materials processing and reduces the potential for impurity introduction for sulfide-based electrolytes through conventional solid-state reaction synthesis method.

Next, the amorphous powder was transformed into pellets by hydraulic cold pressing at various pressures. XRD conducted on pellets (Fig. S4) indicates that the material was still mostly amorphous after hydraulic pressing, confirming that no significant phase or composition change occurred but physical densification. A broad shoulder peak at 25°-35° range is indicative of vitrification intensified with the pressure reflecting the existence of some shortrange order. The morphology, densification, and defects present in

each sample are observed by unpolished cross-section SEM images. (Fig. 8) All samples display a porous morphology structure following the non-isostatic hydraulic pressing process. The densification monotonously improves with increasing pressure, though the benefits become attenuated above 300 MPa. (Fig. 8e) The relative density was normalized with respect to 1.95 g cm⁻¹, a literature value of cold pressed sample measured by using Helium pycnometry.²¹ The relative density values at different pressures are very comparable with literature.⁵ In addition, all samples exhibit a very good reproducibility for pellet formation with error bars less than ±2%.

Electrochemical performance.—Figure 9 displays the ionic conductivity and electronic conductivity of samples evaluated by electrochemical impedance spectroscopy (9-a) and chronoamperometry (9-b), respectively. The Nyquist plot contains a semicircle and a straight line, which represents the classic feature of a blocking electrode measurement. ²⁵ Ionic conductivity values were extracted from the intersection of the semicircle with the *x*-axis, which includes contributions from both bulk and interfaces. Chronoamperometry was performed by applying a step potential of 500 mV and monitoring the transient current response. In each chronoamperometry experiment, there is a sharp spike which quickly attenuates to a steady-state value. The electronic

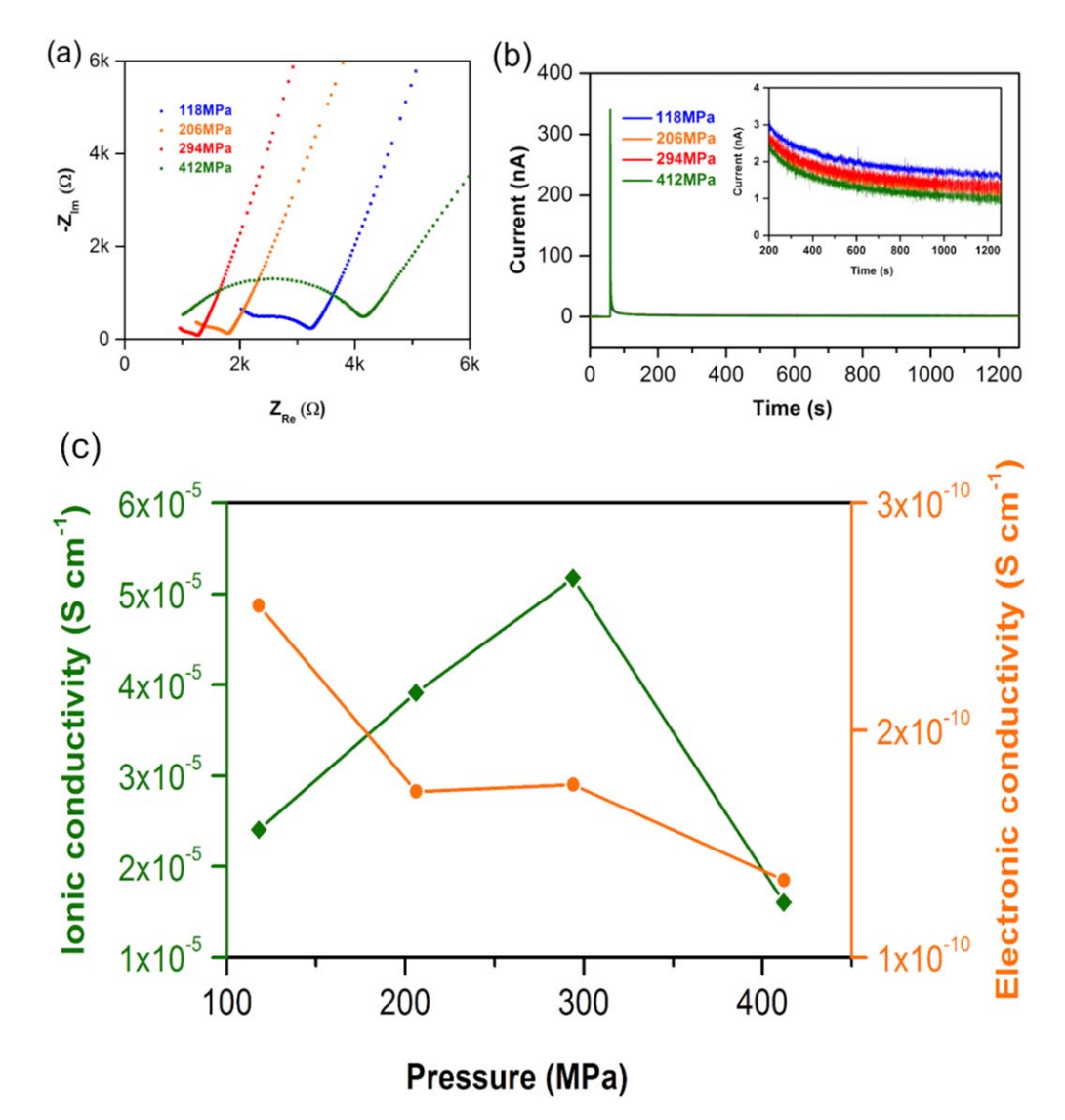


Figure 9. (a) Nyquist plot for glassy electrolyte pellets formed at different pressures, (b) chronoamperometry measurements for pellets formed at different pressures, and (c) summary of the effect of pelletizing pressure on ionic and electronic conductivity.

conductivity was evaluated using Ohm's law and the steady-state current measured after 1200 s. In Fig. 9c, all samples exhibit good ionic conductivity at a level of 10^{-5} s cm⁻¹ indicating good quality of synthesized materials. The linear increase in ionic conductivity with pressure up to 300 MPa is attributed to enhanced densification and vitrification. The optimal value of $5.4 \times 10^{-5} \, \mathrm{S \, cm^{-1}}$ is consistent with previous reports for this material. ^{5,26} Accordingly, the abrupt drop above 300 MPa seems counterintuitive. This drop is attributed to the formation and growth of cracks in these relatively thin (0.7–0.8 mm) pellets.²⁷ Large area imaging of these samples (Fig. S5) shows the presence of large cracks where interface resistance increases significantly at this high pressure. Our hydraulic press was not isostatic and in the absence of polymer additives porosity and crack formation are commonly observed in sulfide materials as reported by other groups.^{28,29} It is noted that some micro cracks may be observed in samples pressed at 100-300 MPa which are highlighted in red circles. Those micro cracks continue growing to form large ones when pressure is over 300 MPa. Besides ionic conductivity, electronic conductivity can have a significant impact on solid-state electrolyte performance though it has been often overlooked. A recent paper published by Han et al. 30 revealed that high electronic conductivity contributes to lithium dendrite formation and penetration into both sulfide and oxide SSEs. It has been proposed that at least six orders of magnitude difference between ionic and electronic conductivity is desired for a good SSE. 31,32 Samples pressed at different pressures exhibit values $\sim\!10^{-10}\,\mathrm{s}\;\mathrm{cm}^{-1}$ which decrease linearly with pressure. These values are exceptionally low compared to the leading literature reports $(10^{-9}-10^{-7} \text{ s cm}^{-1})$.

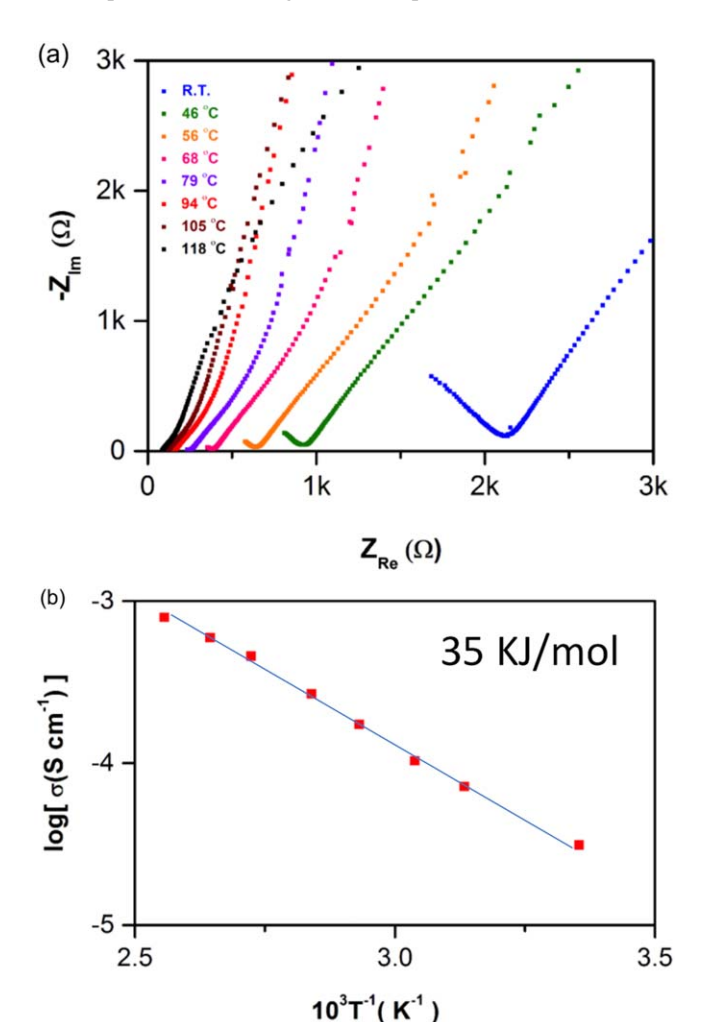


Figure 10. (a) Nyquist plots of 300 MPa cold-pressed pellet at different temperatures and (b) corresponding Arrhenius plot.

More importantly, it has been suggested that the electronic conductivities of the SSE should be lower than 10^{-10} s cm⁻¹ for dendrite-free lithium plating, ^{21,30} our material exhibits values approaching this threshold. Specifically, at 300 MPa pressure the conductivity ratio approaches six orders of magnitude difference, which indicates this material qualifies for a good SSE.

Temperature-dependent EIS was performed on the 300 MPa sample to study kinetics of ion transport from 20 °C to 118 °C. Figure 10a displays Nyquist plots as a function of temperature and the resulting conductivity. The Arrhenius plot (Fig. 10b) is linear with activation energy $E_a = 35 \text{ kJ mol}^{-1}$, which is in good agreement with the literature for $70\text{Li}_2\text{S}-30P_2S_5$ glassy electrolyte.⁵ Again, this activation energy barrier validates the use of our synthesized materials for solid-state electrolyte application.

Conclusions

This work demonstrated the scale up of a solvent-based synthesis of Li₂S using bubble columns and fluidized beds and its application to a model glassy SSE (70Li₂S-30P₂S₅). The synthesis was conducted at 10 g scale with 93% yield of phase-pure Li₂S nanocrystals with a preferred nanoflower morphology. The results of the scale-up process revealed insights into the Li₂S crystallization process during evaporation of ethanol and demonstrates differences that may be encountered between small- and large-scale processing. The nanocrystalline nature of the as-synthesized Li₂S reduced the ball milling time needed to produce the glassy material by at least 70% compared to commercial Li₂S. The cold-pressed SSE possessed ionic conductivity, electronic conductivity, and ion conduction activation energy in good agreement with or better than those reported in the literature, providing validation of the Li₂S synthesis we have presented.

Acknowledgments

This work was supported by the US National Science Foundation through Award 1825470. We also thank Prof. Don Williamson for his help with SAXS measurements and Mark Graas for help with TGA.

ORCID

Colin A. Wolden https://orcid.org/0000-0001-6576-048X

References

- 1. K. Kerman, A. Luntz, V. Viswanathan, Y.-M. Chiang, and Z. Chen, J. Electrochem. Soc., 164, A1731 (2017).
 2. A. C. Luntz, J. Voss, and K. Reuter, J. Phys. Chem. Lett., 6, 4599 (2015).
- Y. Kato, S. Hori, T. Saito, K. Suzuki, M. Hirayama, A. Mitsui, M. Yonemura, H. Iba, and R. Kanno, Nat. Energy, 1, 16030 (2016).
- A. Sakuda, A. Hayashi, and M. Tatsumisago, Sci. Rep., 3, 2261 (2013).
- F. Mizuno, A. Hayashi, K. Tadanaga, and M. Tatsumisago, Solid State Ionics, 177,
- S. Ito, M. Nakakita, Y. Aihara, T. Uehara, and N. Machida, J. Power Sources, 271, 342 (2014).
- S. Choi, J. Ann, J. Do, S. Lim, C. Park, and D. Shin, J. Electrochem. Soc., 166,
- F. Han, T. Gao, Y. Zhu, K. J. Gaskell, and C. Wang, Adv. Mater., 27, 3473 (2015).
- Sigma-Aldrich, (2019), Li₂S Results (Accessed November 14, 2019) www. sigmaaldrich.com/catalog/product/aldrich/213241.
- Y. Zhang, R. Chen, T. Liu, Y. Shen, Y. Lin, and C.-W. Nan, ACS Appl. Mater. Interfaces, 9, 28542 (2017).
- 11. M. Čalpa, N. C. Rosero-Navarro, A. Miura, and K. Tadanaga, RSC Adv., 7, 46499 (2017).
- 12. Y. Wang, D. Lu, M. Bowden, P. Z. El Khoury, K. S. Han, Z. D. Deng, J. Xiao, J.-G. Zhang, and J. Liu, *Chem. Mater.*, 30, 990 (2018).
- 13. B. Xue, B. Fan, B. Li, L. Chen, F. Wang, Z. Luo, X. Zhang, and H. Ma, J. Am. Ceram. Soc., 102, 3402 (2018).
- 14. L. Zhou, K.-H. Park, X. Sun, F. Lalère, T. Adermann, P. Hartmann, and L. F. Nazar, ACS Energy Lett., 4, 265 (2019).
- S. Yubuchi, M. Uematsu, C. Hotehama, A. Sakuda, A. Hayashi, and M. Tatsumisago, J. Mater. Chem. A, 7, 558 (2019).
- 16. S. Yubuchi, M. Uematsu, M. Deguchi, A. Hayashi, and M. Tatsumisago, ACS Appl. Energy Mater., 1, 3622 (2018).
- 17. X. Li, Y. Zhao, A. Brennan, M. McCeig, C. A. Wolden, and Y. Yang, ChemSusChem, 10, 2904 (2017).

- 18. K. Hietala, Y. Zhao, Y. Yang, and C. A. Wolden, Ind. Eng. Chem. Res., 57, 8436
- 19. Y. Zhao, Y. Yang, and C. A. Wolden, ACS Appl. Energy Mater., 2, 2246 (2019).
- 20. X. Li, C. A. Wolden, C. Ban, and Y. Yang, ACS Appl. Mater. Interfaces, 7, 28444 (2015).
- 21. T. A. Yersak, J. R. Salvador, N. P. W. Pieczonka, and M. Cai, *J. Electrochem. Soc.*, 166, A1535 (2019).
- 22. Y. T. Shah, B. G. Kelkar, S. P. Godbole, and W. D. Deckwer, AlChE J., 28, 353 (1982).
- 23. N. Kantarci, F. Borak, and K. O. Ulgen, Process Biochem., 40, 2263 (2005).
- 24. C. Wang, X. Wang, Y. Yang, A. Kushima, J. Chen, Y. Huang, and J. Li, Nano Lett., **15**, 1796 (2015).
- 25. X. Qian, N. Gu, Z. Cheng, X. Yang, E. Wang, and S. Dong, *Electrochim. Acta*, 46, 1829 (2001).
- 26. T. Minami, A. Hayashi, and M. Tatsumisago, *Solid State Ionics*, 177, 2715 (2006).
- 27. J. M. Whiteley, P. Taynton, W. Zhang, and S. H. Lee, *Adv. Mater.*, 27, 6222 (2015).
 28. T. Yersak, J. R. Salvador, R. D. Schmidt, and M. Cai, *ACS Appl. Energy Mater.*, 2,
- 3523 (2019).
- 29. T. Inada, K. Takada, A. Kajiyama, M. Kouguchi, H. Sasaki, S. Kondo, M. Watanabe, M. Murayama, and R. Kanno, *Solid State Ionics*, **158**, 275 (2003). 30. F. Han, A. S. Westover, J. Yue, X. Fan, F. Wang, M. Chi, D. N. Leonard,
- N. J. Dudney, H. Wang, and C. Wang, Nat. Energy, 4, 187 (2019).
- 31. R. Kanno and M. Murayama, J. Electrochem. Soc., 148, A742 (2001).
- 32. B. V. Lotsch and J. Maier, J. Electroceram., 38, 128 (2017).